

Numerical study of high-index-contrast Er:LiNbO₃ photonic wire lasers optically pumped at 980 nm

Md. Sohel Mahmud Sher,¹ Paolo Pintus,^{2,*} and Fabrizio Di Pasquale²

¹Electronics and Communication Engineering Discipline, Khulna University, Khulna 9208, Bangladesh

²Scuola Superiore Sant'Anna, Pisa 56124, Italy

*Corresponding author: paolo.pintus@sssup.it

Received 11 January 2013; revised 5 April 2013; accepted 20 May 2013;
posted 21 May 2013 (Doc. ID 183323); published 21 June 2013

For the first time [to our best knowledge] a high-index-contrast *z*-cut Er:LiNbO₃ photonic wire waveguide laser, optically pumped at 980 nm wavelength, is designed for continuous-wave operation. Waveguide modes and laser characteristics are numerically computed using a developed full vectorial finite-element method based tool. In order to maximize the output power of the laser, the active cavity length and output mirror's reflectivity have been optimized, considering different pump power and waveguide background losses. Efficient laser emission is theoretically predicted at 1531 nm wavelength for the fundamental TE mode and a value of threshold pump power as low as 0.2 mW has been computed. © 2013 Optical Society of America

OCIS codes: (130.0130) Integrated optics; (130.1750) Components; (130.3730) Lithium niobate.
<http://dx.doi.org/10.1364/AO.52.004438>

1. Introduction

Integrated optics based on lithium niobate (LiNbO₃) can provide an attractive technological platform for several communication and sensing applications [1,2]. Erbium doping of LiNbO₃ material can also provide active functionalities, such as optical amplification and lasing at around 1.55 μm, the most attractive wavelength region for fiber-optic communication [3]. Combining the strong electro-optical effect available in LiNbO₃ with the optical gain provided by erbium doping makes Er:LiNbO₃ material attractive for integrated optics and in particular for realizing active photonic switches and modulators.

In the past few years a whole family of low-index-contrast ($\Delta n \sim 1\%$) waveguide lasers of excellent quality has been demonstrated based on Er:LiNbO₃ material. These waveguides have been fabricated by exploiting titanium indiffusion [4–10], zinc oxide

diffusion in MgO:LiNbO₃ [11,12], and carbon ion implantation in Er:LiNbO₃ embedded waveguide [13]. Table 1 reports some examples of erbium-doped laser manufactured using the former approaches. In all those cases, the refractive index contrast between the core and the bulk is quite small, therefore the waveguide core size is relatively large. For Ti and Zn diffused waveguides, the core is usually 5–9 μm wide and 4–6 μm thick, while in C³⁺ implanted waveguide, due to the higher refractive index step, the waveguide cross section is 3 μm large and 3.2 μm deep. An important consequence of the larger core size is the higher pump power threshold. Indeed, it can be proved that the laser threshold is proportional to the effective pump area [14,15] and hence to the physical cross section of the waveguide.

Theoretical analysis has shown that ridge structures can be used successfully to lower the threshold pump power of a low-index-contrast Ti:Er:LiNbO₃ waveguide laser [16]. Such a waveguide shape can indeed increase the confinement factor reducing the pump power threshold. Moreover, strongly guiding LiNbO₃ channel waveguides, characterized by a

Table 1. State-of-the-Art of Er:LiNbO₃ Laser

LiNbO ₃ Waveguide	Fabrication Technique	Erbium Concentration ^a [m ⁻³]	Laser Wavelength [nm]	Pump Wavelength [nm]	Waveguide Loss [dB/cm]	Cavity Length [mm]	Index Contrast ^b Δn	Pump Threshold ^c [mW]	Reference ^d
z-cut	Ti-indiff.	9 × 10 ²⁴	1532 (TE)	1477	0.3	10.5	~1.2 × 10 ⁻²	8 (*)	Brinkmann <i>et al.</i> , 1991, [4]
z-cut	Ti-indiff.	1.2 × 10 ²⁶	1563 (TE) 1576 (TM)	1479	0.7	52.0	~1.2 × 10 ⁻²	25 13	Becker <i>et al.</i> , 1992, [5]
x-cut	Ti-indiff.	1.9 × 10 ²⁶	1531 (TE)	1485	-	30.0	~1.2 × 10 ⁻²	10	Huang <i>et al.</i> , 1994, [6] (**)
z-cut	Ti-indiff.	1.35 × 10 ²⁶	1531 (TE) 1561 (TE)	1484	0.18	70.0	~1.2 × 10 ⁻²	43 20	Baumann <i>et al.</i> , 1996, [3]
x-cut	Ti-indiff.	1.05 × 10 ²⁶	1531.4 (TE)	980	0.4 at λ _s 0.55 at λ _p	29.0	~1.2 × 10 ⁻²	52.5	Amin <i>et al.</i> , 1996, [8]
z-cut	MgO:LiNbO ₃ ZnO-indiff.	-	1531 (TE)	980	-	21.0	~1.9 × 10 ⁻³	30	Huang and Caughan, 1997, [11]
z-cut	C ³⁺ ion implanted	1.0 × 10 ²⁶	1531 (TE)	980	0.2 at λ _s 0.3 at λ _p 0.3 at λ _s , λ _p 0.3 at λ _s , λ _p 1.0 at λ _s , λ _p	20.0 104.0 218.0 58.0	~0.2	25 0.15 0.4 0.2	Sher <i>et al.</i> , 2011, [13] (**)
z-cut	Smart-cut process	1.0 × 10 ²⁶	1531 (TE)	980	1.0 at λ _s , λ _p 2.0 at λ _s , λ _p 2.0 at λ _s , λ _p	98.0 32.0 64.5	~0.7	0.3 0.3 0.5	This work (**)

^aFor erbium-doped diffused waveguide we have considered the maximum erbium concentration at the surface.

^bFor the waveguide made with indiffusion technique, we have considered the maximum contrast between the surface and the bulk. The value for Ti:LiNbO₃ refers to [9,10,15], while the value for ZnO:MgO:LiNbO₃ refers to [12].

^cThe values of pump power thresholds refer to the coupled pump power. The only exceptions are those marked with (*), where [4] reports only the absorbed pump power.

^dThe references marked with (**) refer to theoretical works, while the others are experimental results.

small waveguide cross section and a small bending radius, are more attractive for the development of compact and dense photonic integrated circuits [17,18]. Such small form factor devices can be effectively fabricated by processing a thin smart-cut LiNbO₃ layer, either bonded to a silica (SiO₂) layer on lithium niobate or bonded to Benzocyclobutene (BCB) on a lithium niobate substrate [19]. The smart-cut process is basically a combination of ion implantation and wafer bonding technique. Note that crystal bonding to an SiO₂ cladding layer is preferable due to its lower refractive index ($n_{\text{SiO}_2} \sim 1.46$, $n_{\text{BCB}} \sim 1.55$ and then a higher index contrast can be achieved) and better thermal stability [20].

In this paper, we report numerical analysis of 980 nm pumped continuous-wave lasers, based on high-index-contrast ($\Delta n > 30\%$) z-cut Er:LiNbO₃ photonic wire waveguides, emitting at 1531 nm wavelength. Due to the strong light confinement inside the active waveguide core, very low threshold pump power is expected. For comparison, let us observe that standard laser waveguide structures are characterized by a laser pump power threshold of tens of milliwatts (see Table 1), while photonic wire lasers presented in this work have a threshold that is about a hundred times smaller than for the state-of-the-art lasers in LiNbO₃. Moreover, high-index-contrast Er:LiNbO₃ photonic wire lasers allow higher integration and smaller bending with respect to diffused and ion-implanted laser waveguides, which have a

hundred times larger cross section due to the smaller index contrast (see Table 1). However, such a high-index-contrast demands a very small waveguide cross section in order to support a single guided mode at both pump and laser wavelengths, and therefore, advanced structuring techniques are essential for fabricating low loss waveguides.

Er:LiNbO₃ amplifier and laser devices can be pumped at both 1480 and 980 nm wavelengths. However, theoretical and experimental studies show that these devices can be pumped more efficiently using 980 nm light [11,21]. Moreover, at 980 nm wavelength, pump laser diodes are cheap and readily available. It is also easier to integrate functions like on-chip wavelength division multiplexers for independent pump and signal routing [21]. Therefore, we have decided to pump our laser at 980 nm.

Using our developed numerical tool we investigate the effects of background losses on the lasing performance, pointing out that very low laser thresholds seem to be feasible at low background losses while both the laser and pump lights are considered to be TE polarized. Optimization of the laser cavity has been performed by adjusting the cavity length (L) and the output mirror's reflectivity (R_2) simultaneously, for a fixed pump power. A Bragg grating is assumed as the output mirror, which enables single wavelength laser emission at 1531 nm, i.e., at the region where erbium absorption or emission peaks are typically observed in Er:LiNbO₃.

This paper is organized as follows. Section 2 briefly reports the geometry and modal analysis of our proposed high-index-contrast Er:LiNbO₃ photonic wire waveguide laser. A formulation of the steady-state laser model is outlined in Section 3. In Section 4, we discuss the laser performance and investigate the optimum length of the laser cavity for different background loss and pump power. Section 5 provides a summary and some concluding remarks.

2. Waveguide Geometry and FEM-Based Modal Analysis

The schematic of our specific designed 980 nm pumped z-cut Er:LiNbO₃ photonic wire waveguide laser is presented in Fig. 1. In order to compute the waveguide modes, the cross section is discretized into a contiguous second-order finite-element triangular mesh by using the commercial computer-aided design tool GiD [22], as shown in Fig. 2. Both the doped and undoped LiNbO₃ are assumed to be z-cut and y-propagating, where the extraordinary and ordinary refractive indices of the material are assigned to the vertical (z axis) and horizontal (x axis) directions, respectively.

Our developed full vectorial finite-element method mode solver is based on the Rayleigh–Ritz approach and it can take the material anisotropy well into account [23,24]. The dimension of the waveguide core (0.5 μm × 0.4 μm) is carefully chosen so that only the fundamental mode is guided at both pump (980 nm) and laser (1531 nm) wavelengths. The refractive indices of different materials used in the modal analysis are listed in Table 2.

Note that for a few percentage of erbium doping in LiNbO₃ the refractive index value does not differ in any significant way from the undoped ones [25] at 632.8 nm; also, as the dispersion equation of Er:LiNbO₃ is not available in the literature, we have reasonably assumed the same refractive indices for both doped and undoped LiNbO₃.

Considering the transversal waveguide cross section, the normalized intensity profiles for the quasi-transverse electric modes are reported in Fig. 3.

Both pump and laser modes have been computed and a strong light confinement is noted at 980 nm. Quasi-transverse magnetic modes are also calculated, although they are not shown here.

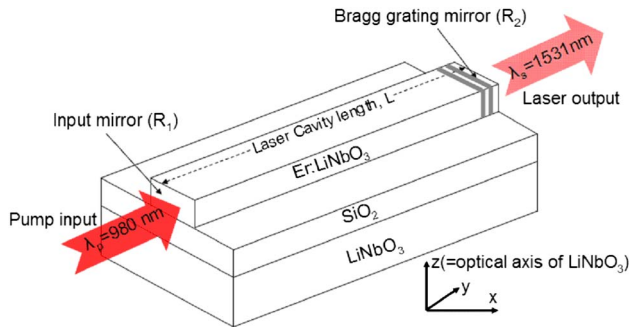


Fig. 1. Schematic diagram of an z-cut y-propagating high-index-contrast Er:LiNbO₃ photonic wire laser.

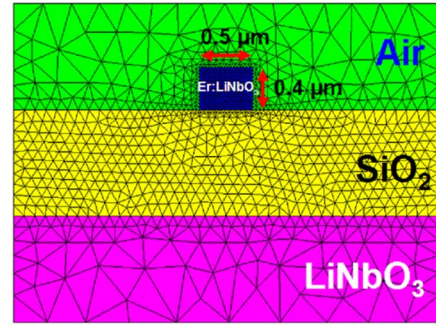


Fig. 2. Transversal cross section of the waveguide is discretized into 2146 second-order finite element triangular mesh, 508 of which are active (i.e., they reside in the Er:LiNbO₃ region).

Since the TE mode at 980 nm has higher absorption cross section (see Table 3), we assumed to excite only the TE mode at the pump wavelength. This can be easily done using a polarization controller between the cavity and the pump. Similarly, at the laser wavelength, the TE mode shows higher emission cross section compared to the TM case (see Table 3). For this reason, we have considered only the TE polarizations in our simulations. Let us observe that considering the TE mode only at 1531 nm is consistent with experimental results, which shows that only the polarization having higher emission cross section will lase [5,6].

3. Theoretical Model

We consider a three-level Er³⁺ laser system pumped at 980 nm. The model takes into account the cooperative upconversion (C_{UP}) from the metastable level (⁴I_{13/2}) and the excited-state absorption (ESA) from the ⁴I_{11/2} energy level, as shown in Fig. 4.

The population rate equations and the conservation laws are described as follows:

$$\frac{\partial n_1}{\partial t} = -(W_{12} + R_{13})n_1 + \left(W_{21} + \frac{1}{\tau_{21}}\right)n_2 + R_{31}n_3 + C_{UP}n_2^2, \quad (1)$$

$$\frac{\partial n_2}{\partial t} = W_{12}n_1 - \left(W_{21} + \frac{1}{\tau_{21}}\right)n_2 + \frac{1}{\tau_{32}}n_3 - 2C_{UP}n_2^2, \quad (2)$$

$$\frac{\partial n_3}{\partial t} = R_{13}n_1 - \left(R_{31} + \frac{1}{\tau_{32}}\right)n_3 + C_{UP}n_2^2, \quad (3)$$

Table 2. Material Refractive Indices

Materials	Refractive Index	
	λ = 980 nm	λ = 1531 nm
Air	1	1
SiO ₂	1.45	1.44
LiNbO ₃ /Er:LiNbO ₃	2.24 (ordinary)	2.21 (ordinary)
	2.16 (extraordinary)	2.14 (extraordinary)

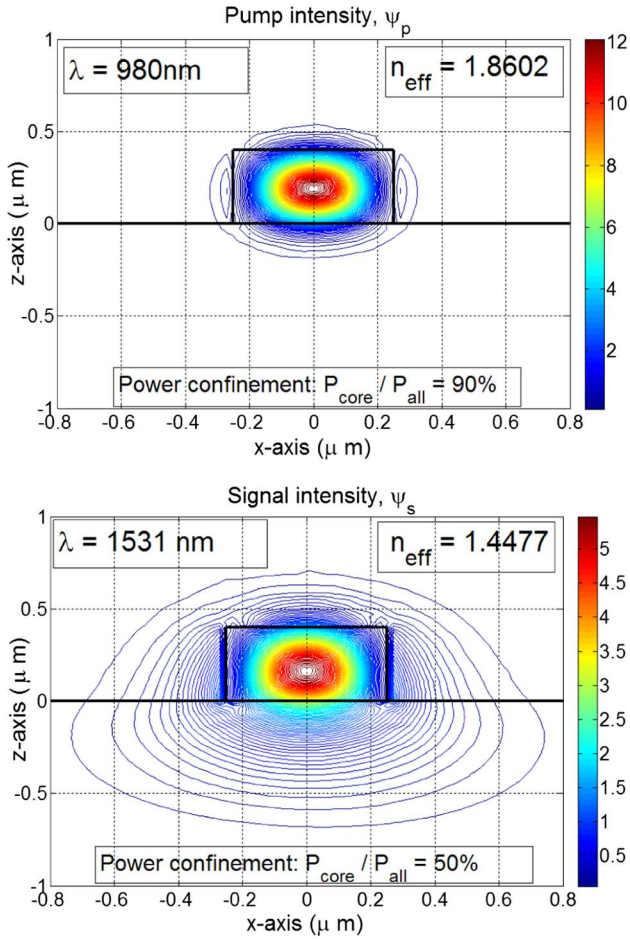


Fig. 3. Normalized intensity profiles ($W/\mu\text{m}^2$) for the QTE modes at pump (top) and signal (bottom) wavelengths computed by our full vectorial FEM code. Mode effective indices (n_{eff}) and power confinements ($P_{\text{core}}/P_{\text{all}}$) are also presented at corresponding wavelengths.

$$N_{\text{Er}} = n_1 + n_2 + n_3, \quad (4)$$

where n_1, n_2, n_3 are the Er^{3+} populations in the energy levels ${}^4I_{15/2}, {}^4I_{13/2}$ and ${}^4I_{11/2}$, respectively. N_{Er} represents the total erbium ions concentration, τ_{ij} is the lifetime of the energy levels (from level i to level j)

and C_{UP} represents the concentration-dependent up-conversion coefficient. The laser and pump induced transition rates, W_{ij} and R_{ij} , are described by the following expressions:

$$W_{ij} = \sum_{k=1}^M \frac{\sigma_{ij}^s(\nu_k)}{h\nu_k} [I_{\text{ASE}}^+(x, y, z; \nu_k) + I_{\text{ASE}}^-(x, y, z; \nu_k)], \quad (5)$$

$$R_{ij} = \frac{\sigma_{ij}^p(\nu_p) I_p(x, y, z; \nu_p)}{h\nu_p}, \quad (6)$$

where M is the number of frequency slots used for the discretization of the absorption and emission cross sections shown in Fig. 5, I_{ASE}^+ and I_{ASE}^- are the copropagating and counterpropagating ASE light intensities, while I_p represents the pump intensity; finally σ_{ij}^s and σ_{ij}^p indicate the absorption ($i < j$) and emission cross sections ($j < i$) at frequencies ν_k for the ASE and ν_p for the pump, respectively.

The steady-state evolution of pump (P_p) and ASE (P_{ASE}^\pm) powers along the propagation direction (y) can be described by the following propagation equations:

$$\begin{aligned} \frac{dP_p(y; \nu_p)}{dy} = P_p(y; \nu_p) \int_A [\sigma_{31}^p(\nu_p) n_3(x, y, z) \\ - \sigma_{13}^p(\nu_p) n_1(x, y, z) - \sigma_{\text{ESA}}^p(\nu_p) n_3(x, y, z)] \\ \cdot \psi_p(x, z) dA - l_p P_p(y; \nu_p), \end{aligned} \quad (7)$$

$$\begin{aligned} \frac{dP_{\text{ASE}}^\pm(y; \nu_k)}{dy} = \pm P_{\text{ASE}}^\pm(y; \nu_k) \int_A [\sigma_{21}^s(\nu_k) n_2(x, y, z) \\ - \sigma_{12}^s(\nu_k) n_1(x, y, z)] \cdot \psi_s(x, z) dA \pm mh\nu_k \Delta\nu_k \\ \times \int_A \sigma_{21}^s(\nu_k) n_2(x, y, z) \psi_s(x, z) dA \mp l_s P_{\text{ASE}}^\pm(y; \nu_k), \end{aligned} \quad (8)$$

where ψ_p and ψ_s are the normalized mode intensity profiles (assumed to be invariant along the y

Table 3. Input Parameter for Er:LiNbO₃ Laser Model

Parameters	Values	Ref.
σ_{12}^s (at 1531 nm)	$1.25 \times 10^{-24} \text{ m}^2$ (TM) $1.93 \times 10^{-24} \text{ m}^2$ (TE)	Huang <i>et al.</i> 1994 [6]
σ_{21}^s (at 1531 nm)	$1.03 \times 10^{-24} \text{ m}^2$ (TM) $1.56 \times 10^{-24} \text{ m}^2$ (TE)	Huang <i>et al.</i> 1994 [6]
σ_{13}^p (at 980 nm)	$0.20 \times 10^{-24} \text{ m}^2$ (TM) $0.88 \times 10^{-24} \text{ m}^2$ (TE)	Huang and Caughan 1996 [26]
σ_{31}^p (at 980 nm)	0 m^2	Veasey <i>et al.</i> , 1997 [21]
σ_{ESA} (at 980 nm)	$1.0 \times 10^{-26} \text{ m}^2$	Veasey <i>et al.</i> , 1997 [21]
τ_{32} (${}^4I_{11/2} \rightarrow {}^4I_{13/2}$)	200 μs	Veasey <i>et al.</i> , 1997 [21]
τ_{21} (${}^4I_{13/2} \rightarrow {}^4I_{15/2}$)	4.3 ms	Huang <i>et al.</i> 1994 [6]
N_{Er}	$1.0 \times 10^{26} \text{ m}^{-3}$	Veasey <i>et al.</i> , 1997 [21]
C_{UP} ($N_{\text{Er}} = 1.0 \times 10^{26} \text{ m}^{-3}$)	$1.0 \times 10^{-24} \text{ m}^3 \text{ s}^{-1}$	Veasey <i>et al.</i> , 1997 [21]
Input mirror R_1	99.9% (at 1531 nm)	Our hypothesis
Output Bragg grating mirror R_2	0%–100% (at 1531 nm)	Our hypothesis

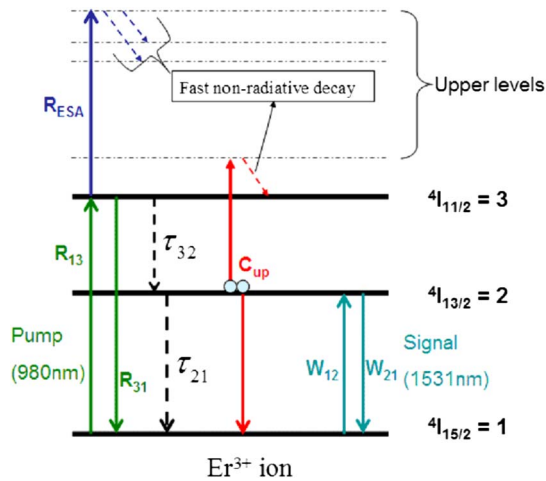


Fig. 4. Schematic energy level diagram of Er^{3+} ions in LiNbO_3 showing different transition rates involved in the calculation. Upper levels are shown with dotted lines to explain the ESA and cooperative upconversion (C_{UP}) mechanism only. In the simulations, the upconversion from $4I_{13/2}$ and ESA from $4I_{11/2}$ have been considered, while those from the upper levels have not been included in the rate equation formulations.

propagation direction) at the pump and ASE wavelengths, respectively, A is the area (in the x - z plane) of the active region ($\text{Er}:\text{LiNbO}_3$) of the waveguide, l_p

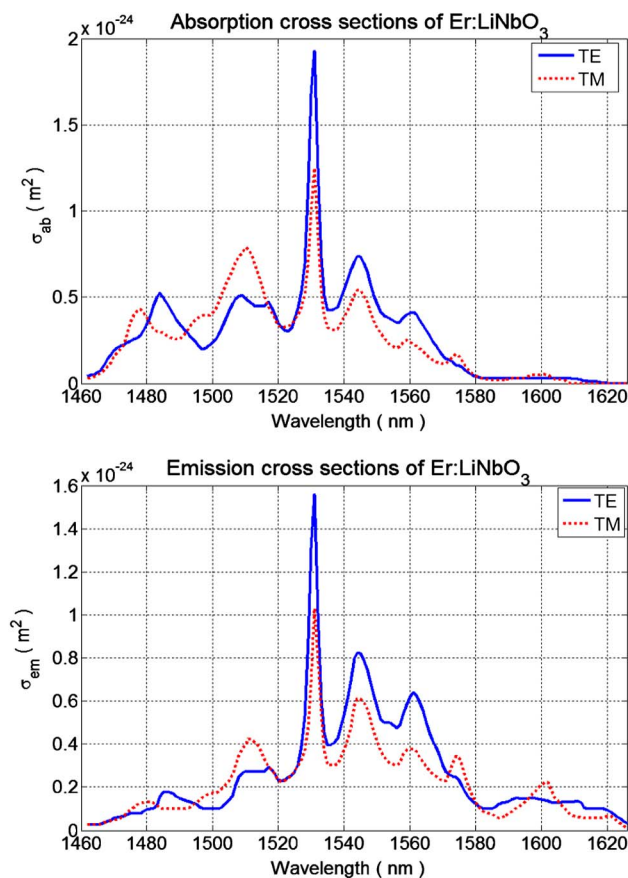


Fig. 5. Absorption (top) and emission (bottom) cross sections of $\text{Er}:\text{LiNbO}_3$ for TE and TM polarizations reproduced after [6] by numerical fitting with 1 nm resolution from 1462 to 1626 nm wavelengths, i.e., $M = 165$.

and l_s are the background losses at the pump and lasing wavelengths, respectively, and m represents the number of guided modes propagating at the laser wavelength, which is 1 because we have considered only the TE fundamental mode [6]. The propagation equations, coupled with the rate equations, are then numerically solved by means of a Runge–Kutta algorithm imposing the following laser boundary conditions:

$$P_{\text{ASE}}^-(L, \nu_s) = R_2 P_{\text{ASE}}^+(L; \nu_s), \quad (9)$$

$$P_{\text{ASE}}^+(0, \nu_s) = R_1 P_{\text{ASE}}^-(0; \nu_s), \quad (10)$$

where L is the length of the laser cavity and R_1 , R_2 are the input dielectric mirror and the output Bragg reflectivity, respectively. The cavity is considered to be nonresonant at the pump wavelength and the laser output power is computed as follows:

$$P_{\text{out}}(\nu_s) = (1 - R_2) \cdot P_{\text{ASE}}^+(L; \nu_s). \quad (11)$$

Mirror R_1 is assumed to be constant in the range 1460–1620 nm and transparent at the pump wavelength. A selective Bragg grating mirror R_2 is used at the laser cavity output, which is equal to zero except for the laser wavelength 1531 nm. Holographic technique can be used to manufacture such a mirror [7].

4. Numerical Results and Discussion

The main issue of the device we have designed is related to the high background loss that has been experimentally observed in such kind of structures. At present, the measured value is about 10 dB/cm for a photonic wire of cross section $1 \mu\text{m} \times 0.73 \mu\text{m}$ [20]. Considering that the technological progress can likely be improved, in our work we have simulated three possible cases for the background loss: 2 dB/cm, 1 dB/cm, and an optimistic 0.3 dB/cm. Even though those values are rather low compared to the state of the art, the use of e-beam lithography instead of optical lithography and additional annealing to smooth the waveguide walls will contribute to loss reduction, as suggested by the authors of [19].

For each of the previous loss values, we consider pump power levels of 1 and 10 mW, and then we compute the laser output power at 1531 nm as a function of both laser cavity length (L) and output mirror's reflectivity (R_2). Laser input parameters listed in Table 3 are the realistic values taken from the literature. Both the pump and the laser modes are considered TE polarized to achieve a higher output power. The results of those simulations are reported in Fig. 6, from where we estimate the optimum pairs (L , R_2) as the one which maximizes the output power for a fixed pump power and background loss values. Considering the optimum pairs (L , R_2), the laser output power versus pump power has been computed

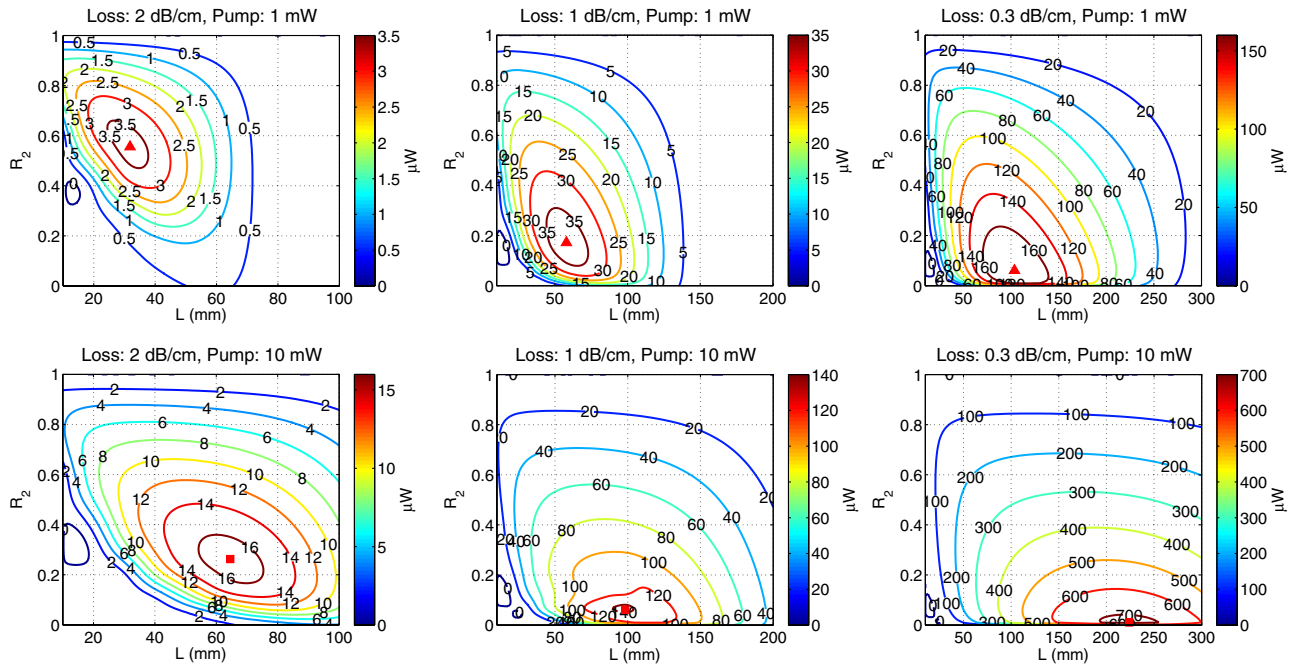


Fig. 6. Constant contour plot of computed laser output power as a function of cavity length (L) and output mirror's reflectivity (R_2) for the pump power of 1 and 10 mW (first and second row, respectively) with the background losses of 2 dB/cm, 1 dB/cm, and 0.3 dB/cm (first, second, and third column, respectively).

and the results are shown in Fig. 7 (the second row in Fig. 7 reports a zoom of the laser characteristics, which clearly identifies the threshold pump power in the different cases). It can be easily seen that as the loss decreases, the optimum laser cavity length increases while the output mirror's reflectivity

decreases. We can see from Fig. 6 that with a background loss of 2 dB/cm (assumed the same at the pump and lasing wavelengths), the optimum laser cavity is 32 mm long with 1 mW pump and 64.5 mm long with 10 mW pump, with an optimum output reflectivity of 55.7% and 26%, respectively.

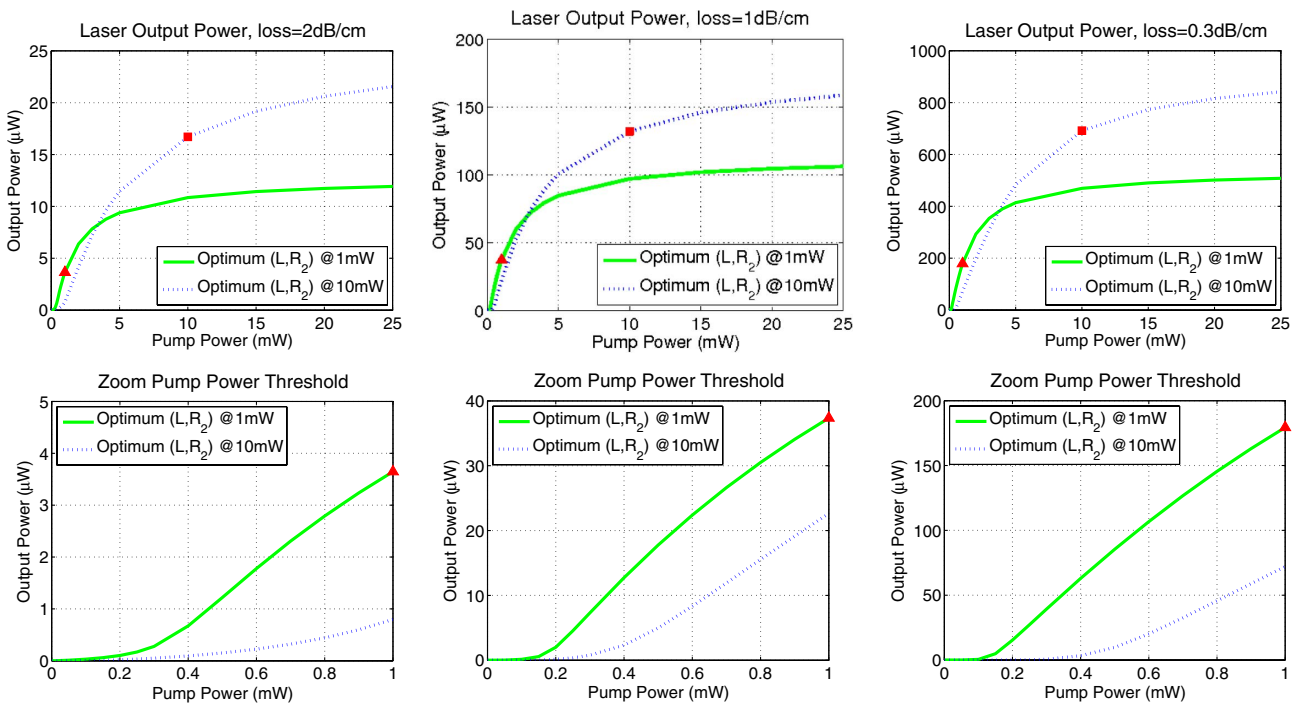


Fig. 7. Laser output power as a function of pump power for optimum laser cavity considering the background losses of 2 dB/cm, 1 dB/cm, and 0.3 dB/cm (first, second, and third column, respectively). The zoomed sections in the second row clearly identify the threshold pump powers.

With 1 dB/cm loss the optimum cavity lengths increase to 58 and 98 mm, with the optimum reflectivities of 17% and 5%, respectively. With the minimum background loss of 0.3 dB/cm, the optimum values are 104, 224 mm, with R_2 equal to 5% and 1%, respectively. However, values of output mirror reflectivity smaller than 5% are nonfeasible. As a consequence, for the last case ($P_{\text{pump}} = 10$ mW and loss = 0.3 dB/cm) we have assumed $R_2 = 5\%$, and we recomputed the optimum cavity length, which is equal to 218 mm.

Let us note that from Fig. 6 $P_{\text{out}} = 0$ when $R_2 = 1$ because all the power is backreflected into the cavity. Vice versa, for $R_2 = 0$ the laser is below the threshold and P_{out} is equal to the amplified spontaneous emission at 1531 nm.

Comparing the results for 1 and 10 mW pump power, we can see that the optimum reflectivity decreases as the pump power increases. Indeed, the higher is the pump power the higher is the optical gain and, as a consequence, a smaller R_2 value allows for larger laser output power. On the other hand, for a fixed pump power we achieve a fixed optical gain. In this case, reducing the waveguide loss produces lower round trip loss, and decreasing R_2 higher laser output power is achieved.

Moreover, considering that lower background losses allow for longer waveguide lengths still ensuring an overall gain greater than the cavity loss. Note that the main benefit of the proposed device is the extremely low threshold pump power. Observing the pictures in the last row of Fig. 7, a few hundred microwatt of pump powers coupled into the wire waveguide are sufficient to turn on the laser effect. In addition, we can also note that the laser thresholds are almost unaffected by each of the background loss values considered.

To better understand this point, let us observe that the threshold pump power is proportional to effective pump area A_{eff} [14–16]. In our waveguide laser A_{eff} results to be 2 orders of magnitude smaller than that reported in [4,5], for an Er-diffused Ti:LiNbO₃ waveguide laser. In the former work, the effective area for the TE mode was 47 μm^2 while we have now computed $A_{\text{eff}} = 0.29 \mu\text{m}^2$. Although the laser wavelengths are different in the two works (1563 and 1531 nm), we can see a similar ratio between the two pump power thresholds and the two effective areas.

In the same figure, we can also note that the output power saturates for relatively small values of pump power. This nonlinear behavior has been experimentally observed in Huang and Caughan [11]. When the ground-state level $^4I_{15/2}$ is completely depleted, the gain reaches its maximum values, then increasing the pump power will not increase the output power.

Let us note that the erbium population n_1 , n_2 , and n_3 in Eqs. (1)–(4) depend on all three coordinates x , y , and z . To be more precise, they depend on the pump power, on the laser power, and on the mode profile $\psi_p(x,y)$ and $\psi_s(x,y)$, shown in Fig. 3. Vice versa,

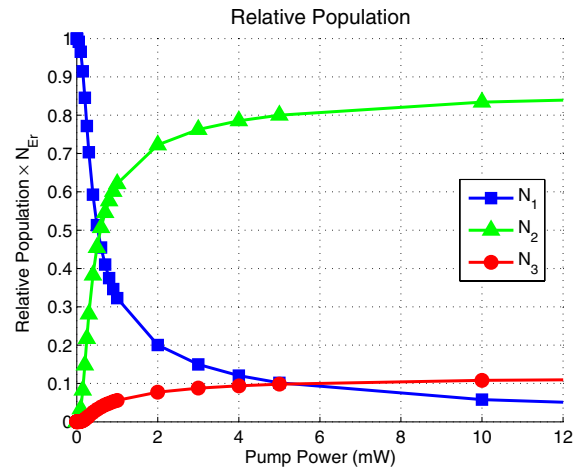


Fig. 8. Relative population of Er ions in the $^4I_{15/2}$ ground state (N_1), in the $^4I_{13/2}$ metastable level (N_2) and in the $^4I_{11/2}$ excited level (N_3). We assumed a background loss of 1.0 dB/cm, a cavity length of 98 mm and $R_2 = 5\%$.

the laser output power is related to the population at $z = L$. To investigate how the energy levels are populated, we introduce the average population at final cross section as

$$N_i = \frac{\int_{\text{Area}} n_i(x,y,z=L) dx dy}{\text{Area}}, \quad i = 1, 2, 3, \quad (12)$$

where Area is the waveguide core size.

Considering a background loss of 1.0 dB/cm, $L = 98$ mm, and $R_2 = 5\%$, in Fig. 8 we have reported the average population N_1 , N_2 , and N_3 in the three-level $^4I_{15/2}$, $^4I_{13/2}$, and $^4I_{11/2}$, at the output laser cross section. As it can be clearly seen, for pump values higher than few milliwatts, the output power starts saturating.

Finally, let us observe that the longitudinal mode spacing is equal to

$$\Delta\nu = \frac{c}{2nL}, \quad (13)$$

where c is the speed of light and n is the effective refractive index of the mode. In our case, for the longest cavity (~ 20 cm) and $n_{\text{eff}}(\lambda = 1531 \text{ nm}) = 1.4477$ (as shown in Fig. 3), we have $\Delta\nu \approx 500$ MHz. As a consequence, we can realistically assume a single longitudinal mode within the narrow Bragg reflector bandwidth, also expecting a narrow laser linewidth.

5. Conclusions

We have theoretically demonstrated the efficient laser performance of a high-index-contrast z -cut Er:LiNbO₃ wire waveguide, optically pumped at 980 nm. Such high-index-contrast LiNbO₃ structures have been recently demonstrated although they still need improvement in terms of background losses. Through our developed numerical tool, we have identified single mode waveguide structure (at both pump and signal wavelengths) and optimized laser

cavities for different background losses and pump power levels. Laser cavity length (L) and output mirror's reflectivity (R_2) have been synchronously adjusted in order to find an optimum pair (L, R_2). Laser output power has been computed for each of the optimum cases considering realistic input parameters. Threshold pump power level of 0.2 mW has been noted for low loss (0.3 dB/cm) waveguides with a maximum output power of around 0.8 mW at an incident pump power level of 25 mW. With a proper technological development, this low-threshold high-index-contrast Er:LiNbO₃ thin film waveguide laser could find interesting applications in both telecom and sensing research fields. Since the optimum laser cavity is rather long, spiral waveguides, characterized by sufficiently large radius to avoid bending losses, could be exploited to achieve a smaller form factor for the active devices, with a great potential for creating ultracompact on-chip laser sources on an LiNbO₃ platform. Note that the same technological process, based on ion implantation and wafer bonding, can be potentially exploited to combine active functions and compact microring devices for fast wavelength switching on the same technological platform.

References

1. S. S. Bosso, "Applications of lithium niobate integrated optic in telecommunication systems," *Proc. SPIE* **3620**, 34–37 (1999).
2. M. Cecchini, F. Beltram, R. Cingolani, S. Girardo, L. Masini, D. Pisignano, and I. Sanzari, "Surface-acoustic-wave driven lab-on-chip technologies," NEST Scientific Report 2007–2009 (University of Dayton, 2009), pp. 71–74.
3. I. Baumann, R. Brinkmann, M. Dinand, W. Sohler, and S. Westenhofer, "Ti:Er:LiNbO₃ waveguide laser of optimized efficiency," *IEEE J. Quantum Electron.* **32**, 1695–1706 (1996).
4. R. Brinkmann, W. Sohler, and H. Suche, "Continuous-wave erbium-diffused LiNbO₃ waveguide laser," *Electron. Lett.* **27**, 415–416 (1991).
5. P. Becker, R. Brinkmann, M. Dinand, W. Sohler, and H. Suche, "Er-diffused Ti:LiNbO₃ waveguide laser of 1563 and 1576 nm emission wavelengths," *Appl. Phys. Lett.* **61**, 1257–1259 (1992).
6. C.-H. Huang, L. M. Caughan, and D. M. Gill, "Evaluation of absorption and emission cross sections of Er-doped LiNbO₃ for application to integrated optic amplifiers," *J. Lightwave Technol.* **12**, 803–809 (1994).
7. W. Sohler, B. K. Das, D. Dey, S. Reza, H. Suche, and R. Ricken, "Erbium-doped lithium niobate waveguide lasers," *IEICE Trans. Electron.* **E88-C**, 990–997 (2005).
8. J. Amin, J. A. Aust, and N. A. Sanford, "Z-propagating waveguide lasers in rare-earth-doped Ti:LiNbO₃," *Appl. Phys. Lett.* **69**, 3785–3787 (1996).
9. S. Fouchet, A. Carencio, C. Daguette, R. Guglielmi, and L. Riviere, "Wavelength dispersion of Ti-induced refractive index change in LiNbO₃ as a function of diffusion parameters," *J. Lightwave Technol.* **5**, 700–708 (1987).
10. D. Kip, B. Gather, H. Bendig, and E. Krätzig, "Concentration and refractive index profiles of titanium- and iron-diffused planar LiNbO₃ waveguides," *Phys. Status Solidi* **139**, 241–248 (1993).
11. C.-H. Huang and L. M. Caughan, "Photorefractive-damage-resistant Er-indiffused MgO:LiNbO₃ ZnO-waveguide amplifiers and lasers," *Electron. Lett.* **33**, 1639–1640 (1997).
12. W. M. Young, M. M. Fejer, M. J. F. Digonnet, A. F. Marshall, and R. S. Feigelson, "Fabrication, characterization and index profile modelling of high-damage resistance Zn-diffused waveguides in congruent and MgOL lithium niobate," *J. Lightwave Technol.* **10**, 1238–1246 (1992).
13. S. M. Sher, P. Pintus, F. Di Pasquale, M. Bianconi, G. B. Montanari, P. De Nicola, S. Sugliani, and G. Prati, "Design of 980 nm-pumped waveguide laser for continuous wave operation in ion implanted Er:LiNbO₃," *IEEE J. Quantum Electron.* **47**, 526–533 (2011).
14. K. Kubodera and K. Otsuka, "Single-transverse-mode LiNdP₄O₁₂ slab waveguide laser," *J. Appl. Phys.* **50**, 653–659 (1979).
15. D. Zhang, C. Chen, J. Li, G. Ding, X. Chen, and Y. Cui, "A theoretical study of a Ti-diffused Er:LiNbO₃ waveguide laser," *IEEE J. Quantum Electron.* **32**, 1833–1838 (1996).
16. J. Liu, Y. Wang, S. Chang, and W. Wang, "Lowering the threshold pump power of Ti:Er:LiNbO₃ laser with ridge structure," *IEEE Photon. Technol. Lett.* **12**, 1204–1206 (2000).
17. A. Guarino, G. Poberaj, D. Rezzonico, R. Degl'Innocenti, and P. Gunter, "Electro-optically tunable microring resonators in lithium niobate," *Nat. Photonics* **1**, 407–410 (2007).
18. M. Koechlin, F. Sulser, Z. Sitar, G. Poberaj, and P. Gunter, "Free-standing lithium niobate microring resonators for hybrid integrated optics," *IEEE Photon. Technol. Lett.* **22**, 251–253 (2010).
19. H. Hu, R. Ricken, and W. Sohler, "Lithium niobate photonic wires," *Opt. Express* **17**, 24261–24268 (2009).
20. H. Hu, R. Ricken, and W. Sohler, "High refractive index contrast ridge waveguides in LiNbO₃ thin film," in *Proceedings of the European Conference on Lasers and Electro-Optics and the European Quantum Electronics Conference (CLEO-EQEC)*, Vol. **1** (2009), pp. 14–19.
21. D. L. Veasey, J. M. Gary, J. Amin, and J. A. Aust, "Time-dependent modeling of erbium-doped waveguide lasers in lithium niobate pumped at 980 and 1480 nm," *IEEE J. Quantum Electron.* **33**, 1647–1662 (1997).
22. GiD <http://gid.cimne.upc.es/>.
23. A. Konrad, "High-order triangular finite elements for electromagnetic waves in anisotropic media," *IEEE Trans. Microwave Theory Tech.* **25**, 353–360 (1977).
24. J. Jin, *The Finite Element Method in Electro-magnetics* 2nd ed. (Wiley, 2002).
25. http://www.roditi.com/Optical/Erbium_Lithium.html.
26. C.-H. Huang and L. M. Caughan, "980 nm-pumped Er-doped LiNbO₃ waveguide amplifiers: a comparison with 1484 nm pumping," *IEEE J. Sel. Top. Quantum Electron.* **2**, 367–372 (1996).